PNAS

RESEARCH ARTICLE | ENGINEERING

Monofluorinated acetal electrolyte for high-performance lithium metal batteries

Elizabeth Zhang[a,b,1], Yuelang Chen[a,c,1], John Holoubek[a,b], Zhiao Yu[a,c], Wenbo Zhang[b], Hao Lyu[a], Il Rok Choi[a,b], Sang Cheol Kim[b], Chad Serrao[b], Yi Cui[b,d,2], and Zhenan Bao[a,2]

Affiliations are included on p. 11.

Edited by Catherine Murphy, University of Illinois at Urbana-Champaign, Urbana, IL; received September 24, 2024; accepted December 2, 2024

High degree of fluorination for ether electrolytes has resulted in improved cycling stability of lithium metal batteries due to stable solid electrolyte interphase (SEI) formation and good oxidative stability. However, the sluggish ion transport and environmental concerns of high fluorination degree drive the need to develop less fluorinated structures. Here, we depart from the traditional ether backbone and introduce bis(2-fluoroethoxy)methane (F2DEM), featuring monofluorination of the acetal backbone. High coulombic efficiency and stable long-term cycling in Li||Cu half cells can be achieved with F2DEM even under fast Li metal plating conditions. The performance of F2DEM is further compared with diethoxymethane (DEM) and 2-[2-(2,2-difluoroethoxy)ethoxy]-1,1,1-trifluoroethane (F5DEE). A significantly lower overpotential is observed with F2DEM, which improves energy efficiency and enables its application in high-rate conditions. Comparative studies of F2DEM with DEM and F5DEE in anode-free lithium iron phosphate ($LiFePO_4$) LFP pouch cells and high-loading LFP coin cells further show improved capacity retention of F2DEM electrolyte, demonstrating its practical applicability. More importantly, we also extensively investigate the underlying mechanism for the superior performance of F2DEM through various techniques, including X-ray photoelectron spectroscopy, scanning electron microscopy, cryogenic electron microscopy, focused ion beam, electrochemical impedance spectroscopy, and titration gas chromatography. Overall, F2DEM facilitates improved Li deposition morphology with reduced amount of dead Li. This enables F2DEM to show superior performance, especially under higher charging and slower discharging rate conditions.

monofluorination | acetal electrolyte | lithium metal battery

Significance

Lithium metal batteries (LMBs) hold tremendous potential for next-generation energy storage due to their high energy density, but their commercial adoption is hindered by poor stability and safety concerns. This work introduces an electrolyte design strategy that uses minimal fluorination combined with a modified molecular backbone structure to achieve stable, high-performance LMBs. Unlike previous approaches that relied on heavy fluorination—which raises environmental concerns and reduces ion transport—this electrolyte achieves excellent performance with just two fluorine atoms per molecule. The electrolyte enables faster charging, better stability, and reduced formation of dead lithium compared to existing solutions. This work demonstrates that strategic molecular design can achieve optimal battery performance.

Lithium metal has emerged as a highly promising battery anode material with its high theoretical specific capacity (3,860 mAh g^{-1}) and low standard reduction potential [−3.04 V vs. standard hydrogen electrode (1–3)]. Despite their potential benefits, lithium metal batteries (LMB) still suffer from low coulombic efficiency (CE) and poor cycling stability (4–6). Generally, if 1,000 stable cycles with more than 90% capacity retention is desired, the averaged CE would have to be at least 99.99% (7). One major factor that significantly impacts the CE is the formation of a stable SEI layer on the surface of the anode. The SEI layer is critical for preventing further reactions between the anode and electrolyte (8, 9). However, SEI is prone to cracking during cycling, which results in mossy Li growth, the formation of "dead Li", irreversible loss of lithium inventory, and excess SEI formation (6).

Among the different strategies to modify the SEI formation and improve CE, rational electrolyte design is essential (4, 10–12). Some of the electrolyte engineering strategies that have been extensively investigated in recent years include high-concentration electrolytes (13), localized high-concentration electrolytes (LHCEs) (14, 15), additive design (16), mixed solvent systems (17, 18), dual-salt-dual-solvent electrolytes (19, 20), and single-salt-single-solvent electrolytes (12, 21–23). Among the various electrolyte systems, fluoroethers have emerged as a promising class of solvent for lithium metal batteries (12, 22–28). Solvent fluorination not only modifies solvation structure for favorable SEI formation but also improves oxidation stability with high-voltage cathodes.

To address the aforementioned issues, we designed and synthesized bis(2-fluoroethoxy)methane (F2DEM). The weakened solvation of the acetal backbone and monofluorination contribute synergistically to the enhanced performance. More specifically, the formation of a fluorine-rich interphase that effectively stabilizes the Li metal anode, and the moderately weakened solvation that improves transport properties. This synergistic effect of low-degree fluorination results in both improved conductivity and superior interfacial stability. Compared with the two reference electrolytes, 2M LiFSI/diethoxymethane (DEM) and 1.2M LiFSI/2-[2-(2,2-Difluoroethoxy)ethoxy]-1,1,1-Trifluoroethane (F5DEE), 2M LiFSI/F2DEM showed

A preprint version of this article is available on arXiv. (https://arxiv.org/abs/2305.19580).

Competing interest statement: This work is part of U.S. Provisional Application No.63/339,300 filed on May 6, 2022 (priority date of International Application No.PCT/US2023/021234).

This article is a PNAS Direct Submission.

[1]E.Z. and Y. Chen contributed equally to this work.

[2]To whom correspondence may be addressed. Email: yicui@stanford.edu or zbao@stanford.edu.

This article contains supporting information online at https://www.pnas.org/lookup/suppl/doi:10.1073/pnas.2418623122/-/DCSupplemental.

Published January 7, 2025.

excellent CE and stable long-term cycling in Li||Cu half cells. A significantly lower overpotential was also observed with F2DEM, which improves the energy efficiency and enables its application in high-rate conditions. Additionally, improved capacity retention was observed with F2DEM in anode-free LFP pouch cells and high-loading LFP coin cells, surpassing that of our previously reported high-performing F5DEE electrolyte. Further studies on the capacity loss mechanisms show improved Li deposition morphology in F2DEM electrolyte, which greatly reduces dead Li formation.

Molecular Design Strategy

Ether solvents have demonstrated noticeable potential as electrolyte solvents in LMB due to their better stability with the Li anode as compared to carbonates (21, 29–31). However, their low oxidative stability poses challenges to applications in high-voltage batteries. To improve the cathode stability of ether electrolytes, incorporating electron-withdrawing fluorine atoms was found to deepen the HOMO energy level (12, 22, 24–28). While a higher degree of fluorination (i.e., CF_2, CF_3) is expected to yield a higher oxidative stability, they are often accompanied by slower ion transport that leads to limited application in faster rate conditions (22). Environmental concerns of highly fluorinated compounds also drive the need to develop monofluorinated alternatives (32).

Monofluorinated ethers have been reported with ethylene glycol ether backbone, namely 1,2-bis(2-fluoroethoxy) ethane (FDEE) (28). However, when used as the single solvent with LiFSI, poor Li cycling stability was observed. To stabilize the CE of monofluorinated ethers, previous approach relied on a LHCE design to reduce solvent participation in interfacial reactions and derive a more stable inorganic-rich SEI (28). However, the LHCE approach not only requires highly fluorinated compounds with great environmental concerns, but the addition of highly fluorinated diluents can also hinder the ion transport and lower the overall conductivity of the electrolyte. These drawbacks motivate us to test the feasibility of designing a single-solvent system that achieves excellent Li cycling performance even with low degree of fluorination.

Our recent work suggested that the acetal structure can effectively weaken the solvation power (33). Considering this, our design steers away from the traditional ether backbone and uses an acetal backbone as the main approach to weaken the solvation strength. We hypothesize that this will enable more stable cycling even in monofluorinated systems, without having to increase the concentration of the electrolyte or introducing highly fluorinated diluent. Based on these design principles, F2DEM is synthesized with monofluorination of the acetal backbone (Fig. 1), which ensures stability at both the anode and cathode side, in addition to maintaining good ionic conductivity.

Electrolyte Solvation and Transport Properties

Adequate ion transport is essential to a high-performing LMB system, and Li salt concentrations can affect the ionic conductivity (34). Therefore, it is necessary to first determine the optimal salt concentration before proceeding with cell cycling and characterizations. Electrolyte solutions were obtained by mixing LiFSI with F2DEM at 1.2 to 3 mol of LiFSI in per liter of solvent, and ionic conductivities were measured with and without a separator. Note that here, we will refer to mol LiFSI/L solvent as molarity (M), their corresponding mol LiFSI/L solution values can be found in Supplementary Table 1. The setup without a separator allows us to measure the intrinsic conductivity of the electrolytes, while conductivity with separator better mimics the condition in realistic cells. For the setup with separator, SS||SS coin cells were assembled with Celgard 2325 separator swelled by different concentrations F2DEM. To measure the conductivity without separator, Swagelok cells were used. The ionic conductivity with separator peaked at around 2M LiFSI/F2DEM (Fig. 2*A*). In the separator-free Swaglok setup, 2M remained the optimal concentration for high ionic conductivity (Fig. 2*B*). Compared to the conductivity of DEM and F5DEE, F2DEM shows the higher conductivity across all the different concentrations (*SI Appendix*, Fig. S4). It is interesting that monofluorination leads to conductivity increase, while fluorination has been generally expected to lead to decreased conductivity. We hypothesize that strategic fluorination can potentially modify the electron density distribution around the ether oxygen atoms, resulting in optimized Li+-solvent coordination strength that facilitates more dynamic solvation shell exchange. The transport numbers of different concentrations were also measured for F2DEM. Higher transport number is generally desired as a higher fraction of the current is carried by Li^+. As shown in Fig. 2*C*, the measured values for all concentrations (>0.4) are comparable to the transport number commonly reported in ether electrolytes (12, 22, 27). Values used for calculations for the ionic conductivity with and without separators are documented in *SI Appendix*, Tables S3 and S4. The detailed current vs. time and EIS plots for transport number calculation are included in *SI Appendix*, Figs. S16–S19.

The viscosities of the three electrolytes are measured with and without LiFSI salt added (Fig. 2*D* and *SI Appendix*, Fig. S3). When no salt is added to the solvent, F5DEE has the highest viscosity, followed by F2DEM and DEM. This is likely due to the high degree of fluorination in F5DEE, which can potentially enhance the intermolecular interactions between the solvent molecules. When salt is added to the system, 2M LiFSI/F2DEM shows higher viscosity compared to 2M LiFSI/DEM and 1.2M LiFSI/F5DEE, which are the optimal concentration for CE measurements, respectively. It should be noted that 2M LiFSI/F5DEE

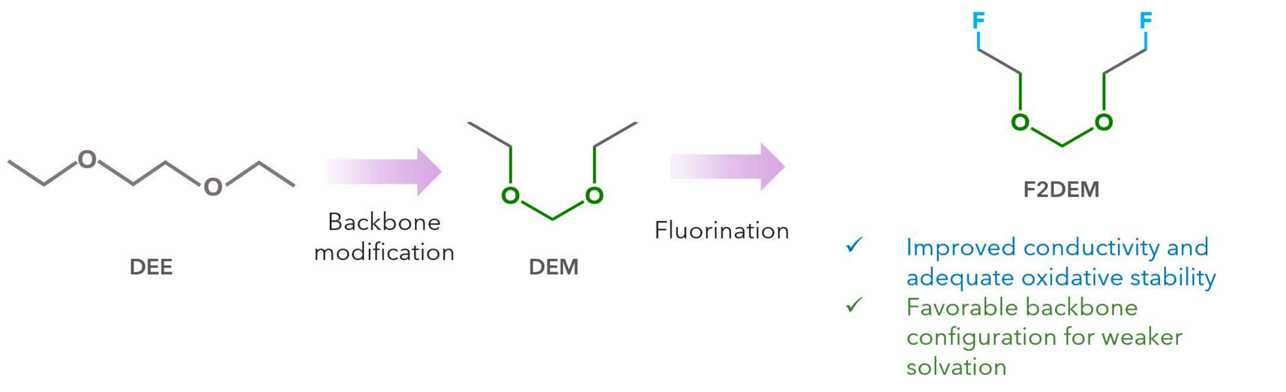

Fig. 1. Molecular design of F2DEM that harvests the benefits of enhanced oxidative stability of monofluorination and weakened solvation of acetal backbone.

 https://doi.org/10.1073/pnas.2418623122

still shows the highest viscosity, although this concentration is not used for battery cycling. Regardless of the higher viscosity, 2M LiFSI/F2DEM still shows the highest ionic conductivity among the three electrolytes.

Next, we study solvation environment of F2DEM through solvation free energy measurement previously developed by Kim et al. (35) Note that the $\Delta G_{solvation}$ values are in reference to 1M LiFSI in DEC. Compared to a solvation free energy of -8.05 kJ mol^{-1} measured in DEE, the solvation power decreases drastically in DEM ($\Delta G_{solv} \approx 14$ kJ mol^{-1}) due to its acetal structure (Fig. 2*E*). Fluorination further weakens the solvation in F2DEM. With the backbone effect, F2DEM can achieve similar solvation energy as F5DEE even with low degree of fluorination. Raman spectroscopy is also used to compare the relative amount of contact ion pairing and aggregates in each electrolyte system. As shown in Fig. 2*F*, more contact ion pairing and aggregation is observed in both 1.2M F5DEE and 2M F5DEE, followed by 2M F2DEM and 2M DEM. This trend resembles what we observed with solvation free energy measurement.

As previously mentioned, we trace the origins of the weakened solvation in F2DEM to its acetal backbone. To verify this effect, we conducted a computational study based on molecular dynamics (MD) and DFT to identify the optimal binding configurations of Li^+ in each electrolyte. As shown in *SI Appendix*, Figs. S1 and S2, the number of FSI^- and solvent coordinated to Li^+ in the primary solvation sheath via MD matches the trend observed with solvation free energy measurement and Raman spectroscopy (Fig. 2*F*). The highly fluorinated 1.2M F5DEE is predicted to exhibit locally

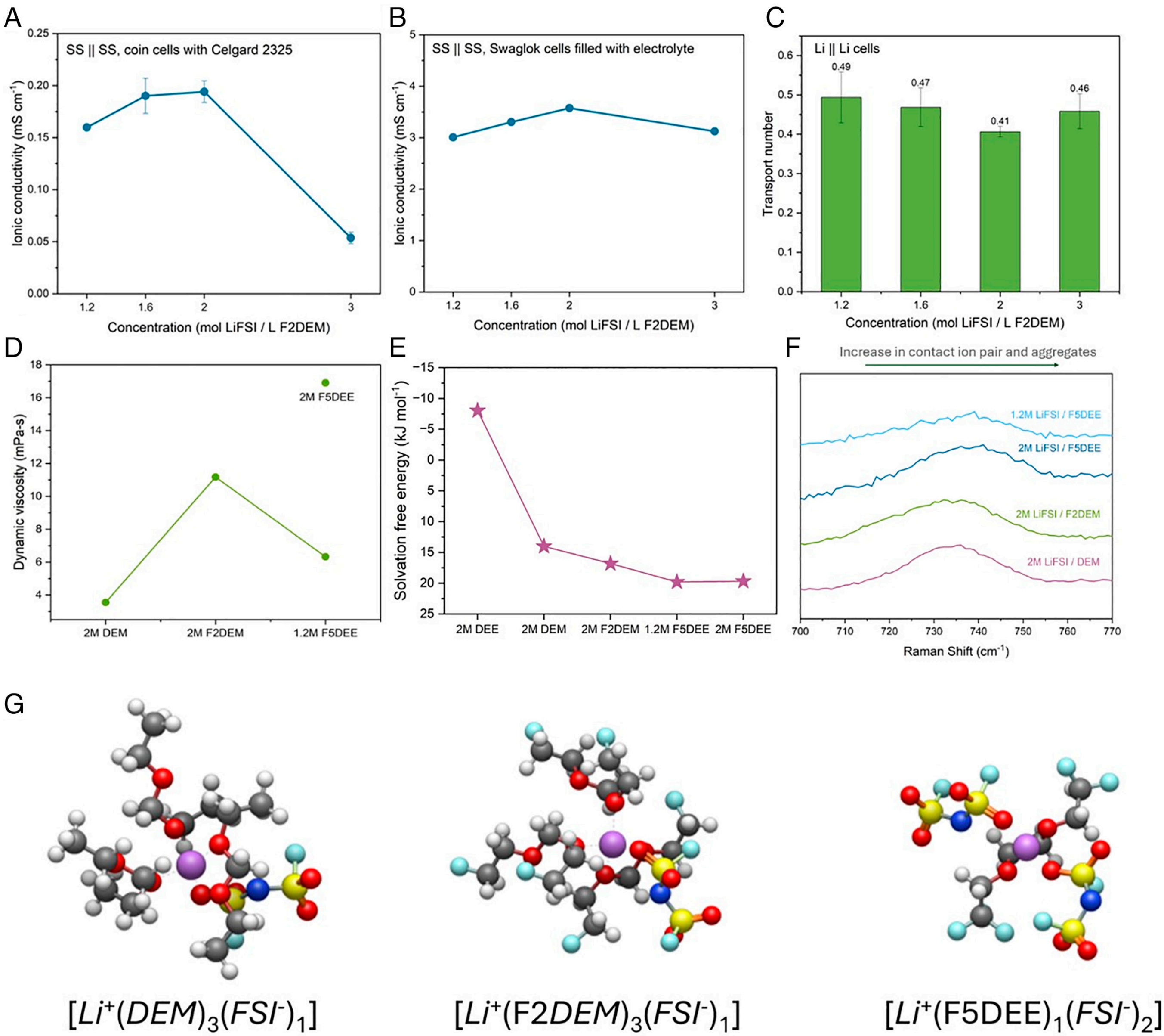

Fig. 2. The transport properties of F2DEM. (*A*) Ionic conductivity of F2DEM measured with Celgard 2325 separator in SS||SS cells across four different concentrations. The ionic conductivity values are averaged among three repeated cells and the SD are shown on the plot. (*B*) The intrinsic ionic conductivity without a separator measured with Swaglok cells across four different concentrations. (*C*) Transport numbers measured in Li||Li symmetric cells for the four different concentrations. The transport numbers are averaged between two repeated cells and the SD are shown on the plot. (*D*) Dynamic viscosity of 2M LiFSI/solvent for DEM, F2DEM, and F5DEE. The viscosity for 1.2M LiFSI/F5DEE is also shown. (*E*) The solvation free energy of DEE, DEM, F2DEM, and F5DEE at 2M concentration measured according to the method outlined in ref. 41. The solvation free energy of 1.2M LiFSI/F5DEE is also shown to reflect property of the electrolyte used during cycling. (*F*) Raman spectroscopy of 2M LiFSI/DEM, F2DEM, F5DEE and 1.2M LiFSI/F5DEE, showing increase in contact ion pairing and aggregates with fluorination. (*G*) Density functional theory (DFT) of DEM, F2DEM, and F5DEE showing gauche configuration of DEM and F2DEM.

aggregated solvation shells with an average of ~2 FSI^- per Li^+, whereas the 2M F2DEM and 2M DEM are predicted to contain contact-ion pair structures with an average FSI^- coordination number of 1. The solvation population analysis showing the distribution of different Li^+ solvates is shown in *SI Appendix*, Fig. S15. Increased anion coordination can be seen with F2DEM compared to DEM. However, due to lower degree of fluorination, the anion participation in the solvation shell is not as pronounced in F2DEM compared to F5DEE (22). We then apply DFT to these predicted solvation clusters to gain a more precise understanding of the local configuration of solvation components (Fig. 2*G*). After optimization, we predict that the gauche configuration is preserved in the F2DEM and DEM systems, resulting in monodentate coordination. Overall, the reduced fluorination degree in F2DEM can maintain good ionic conductivity, improving its transport properties while achieving moderate solvation.

Electrochemical Stability

Overpotential is a critical parameter in LMB as it is directly related to the high-rate performance and energy efficiency of the system. To assess the overpotential of F2DEM, Li||Li symmetric cells were made with thick Li (750 μm) on both sides. The cells were cycled under various current densities. With a capacity of 3 mAh cm^{-2} for each cycle, the current density was gradually increased from 1 mA cm^{-2} to 8 mA cm^{-2}, where the cells were cycled 10 times under each current density. As shown in Fig. 3*A*, the overpotential of 2M LiFSI/F2DEM is roughly 50% less than that of 1.2M LiFSI/F5DEE under all current densities. Under a current density of 1 mA cm^{-2}, an overpotential of around 55 mV was observed for F5DEE, similar to our previous report (22). The overpotential of F2DEM, however, is only around 30 mV. This significant drop in overpotential suggests a much higher energy efficiency of F2DEM over F5DEE. This setup also simultaneously assesses the fast-charging capability of the F2DEM electrolyte. Soft short, however, was observed for both F2DEM and F5DEE starting around 6 mA cm^{-2}.

Next, we investigate the performance of 2M LiFSI/F2DEM in Li||Cu half cells as compared to 1.2M LiFSI/F5DEE and 2M LiFSI/DEM. The average CE was first evaluated by the Aurbach method in Li||Cu half cells (36, 37) (Fig. 3*B*). Based on this standard protocol, 5 mAh cm^{-2} of Li was first deposited onto the Cu foil as Li reservoir. This was followed by 10 subsequent cycles of plating and stripping at 0.5 mA cm^{-2} for 1 mAh cm^{-2}. Finally, all deposited Li was stripped from Cu, and the total capacity recovered was divided by the amount deposited to obtain the CE. The average CE of F2DEM was measured as 99.5 % for four cells, which is similar to the 99.5% (3 cells) previously reported with F5DEE (22) and higher than 99.2% (4 cells) with DEM.

Furthermore, we corroborate these observations through long-term cycling of Li||Cu half cells. To probe the long-term cycling stability, the Cu surface was first conditioned by cycling between 0 and 1 V at 0.2 mA cm^{-2} for 10 cycles. For long-term cycling, 1 mAh cm^{-2} of Li was plated onto Cu at 0.5 mA cm^{-2} and stripped to 1 V at a rate of 0.5 mA cm^{-2} (Fig. 3*C* and *SI Appendix*, Fig. S5*A*). Excluding the activation cycles, the average CE of F2DEM in the first 5 to 50 cycles (99.4%) was also higher than that of F5DEE and DEM (both at 99.3%). However, under this less harsh condition, F5DEE appears to have fewer number of activation cycles (number of cycles to reach 99%) as compared to F2DEM, which contrasts with the later experiments under faster charging conditions. Similar experiments were carried out under a faster charge and slower discharge condition (1 mA cm^{-2} plating, 0.4 mA cm^{-2} stripping) with a higher capacity (2 mAh cm^{-2}) to further evaluate the fast-charging capabilities of F2DEM. Under this harsher condition, a more distinct difference can be observed among the three different electrolytes. F2DEM showed a superior cycling stability with a higher CE over 250 cycles compared with F5DEE and DEM (Fig. 3*D* and *SI Appendix*, Fig. S5*B*). Compared to the long-term cycling at 0.5 mA cm^{-2}, this fast plating and slow stripping condition requires more number of cycles to reach stable cycling at 99% for all three electrolytes. However, a more distinct difference can be observed. While F2DEM took less than 10 cycles to reach 99% CE, F5DEE took over 25 cycles to establish a stable SEI and DEM fails to achieve a stable cycling over 99%. This indicates that less capacity was lost during the initial cycles toward the establishment of a stable SEI in F2DEM. This is highly desirable for anode-free cells with limited Li supply.

Considering the modified solvation environment and addition of electron withdrawing fluorine atoms in F2DEM molecules, we would expect an improved oxidative stability of the 2M F2DEM. To corroborate the oxidative stability enhancement of F2DEM upon fluorination, we carried out LSV on the three different electrolytes. To best mimic the realistic full cell cycling environment, Al was first chosen as the working electrode. Sweeping up to 7 V at 1 mV s^{-1}, the resulting leakage current would allow us to evaluate the corrosion of Al current collector (38, 39). With this setup, we observed a leakage current onset at around 6 V for both F2DEM and DEM (Fig. 3*E*). The delayed voltage onset around 6.5 V for F5DEE is likely because of its increased degree of fluorination, which results in a higher oxidative stability.

In addition to LSV, the electrode/electrolyte stability is further assessed through voltage-holding experiments in the Li||Al cell setup. In this case, the voltage was slowly increased from an open circuit to 4.4 V at a scan rate of 1 mV s^{-1}, then the cells were held at 4.4 V for an extended period of time, and the corresponding leakage current was monitored. In this case, no significant leakage current should be observed while holding at 4.4 V if a stable passivation layer was established on the Al surface (21). As shown in Fig. 3*F*, we did not observe a significant leakage current for all three electrolytes. Overall, the passivation of Al is relatively stable at 4.4 V for the tested systems.

LSV experiments were also conducted with Pt working electrode. Unlike the Al cathode current collector, no passivation reactions occurred on the Pt surface. With the absence of a passivating layer, the onset voltage is expected to decrease for all three electrolytes. As shown in Fig. 3*G*, the leakage current was observed at an onset voltage of around 4 V for F2DEM, which is higher than the 3 V observed with DEM. With a higher degree of fluorination in F5DEE, it expectedly shows a higher onset voltage at around 4.5 V. This trend corroborates our hypothesis that increasing the degree of fluorination enhances the oxidative stability and agrees well with the previous research (22).

Pouch Cell Performance

The performance of 2M LiFSI/F2DEM was further assessed in Cu||LFP anode-free pouch cells, with a voltage range from 2.5 V to 3.65 V. Various charging and discharging rates were implemented to fully assess the pouch cell performance of F2DEM (1C = 200 mA or 2 mA cm^{-2}). Note that the nominal capacity at a C/3 charge rate was 210 mAh, or 2.1 mAh cm^{-2}, and the electrolyte loading was 0.5 mL. We first studied the performance of 2M LiFSI/F2DEM under C/2 charge and C/5 discharge rate, significant improvement in discharge capacity and CE was observed in 2M LiFSI/F2DEM compared to 1.2M LiFSI/F5DEE (Fig. 4 *A* and *B*). This is the more

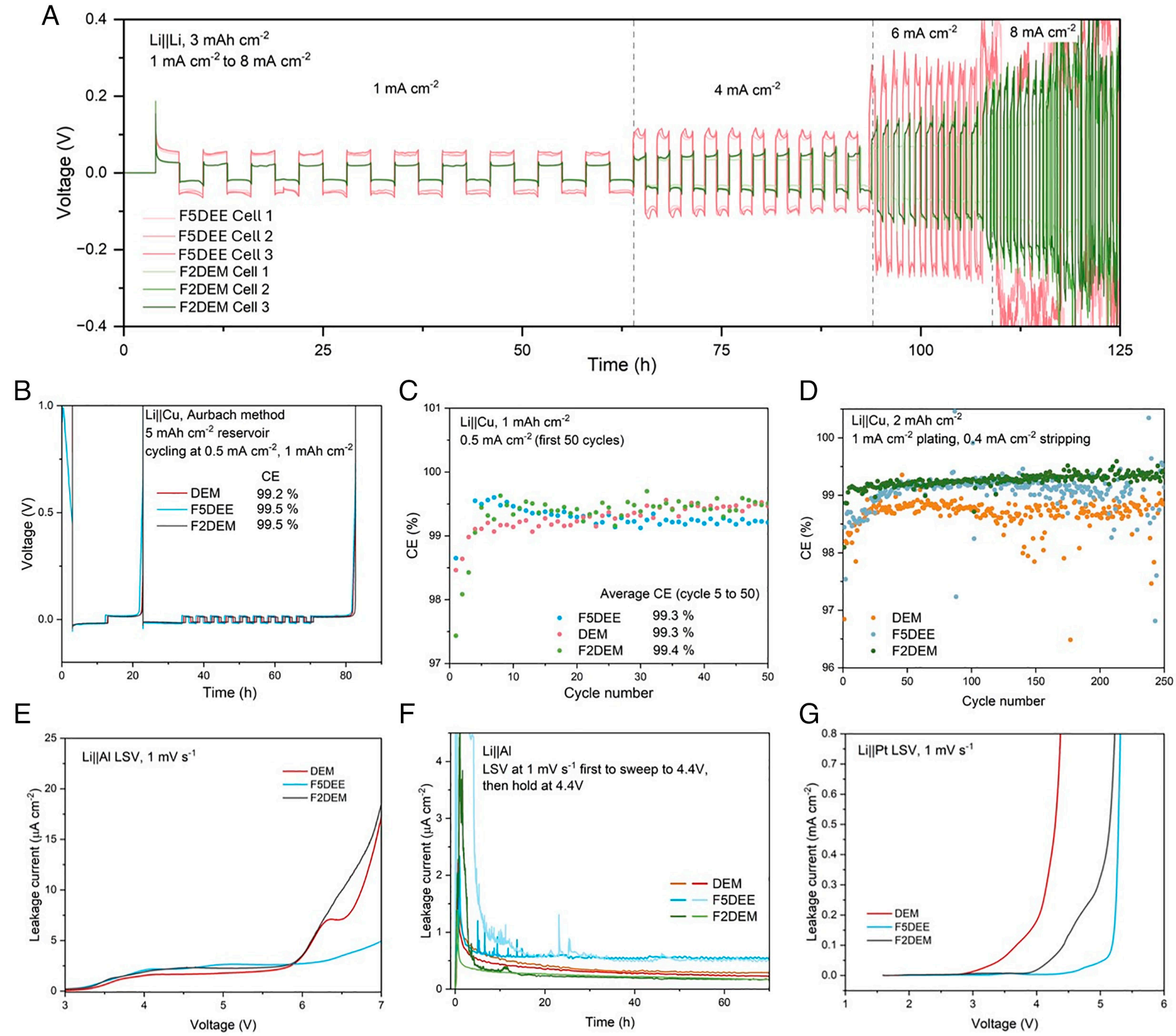

Fig. 3. Electrochemical stability of 2M LiFSI/F2DEM compared with 2M LiFSI/DEM and 1.2M LiFSI/F5DEE. (*A*) Representative Li||Li symmetric cells cycled at increasing current densities (1 mA cm^{-2} to 8 mA cm^{-2}) and 3 mAh cm^{-2} capacity. The cells are cycled 10 times under each current density. Three repeated cells are shown for each electrolyte. (*B*) The CE measurements of the three electrolytes based on the modified Aurbach method (36). The CE was averaged among four cells for F2DEM and DEM. For F5DEE, the CE was averaged between two cells. (*C*) Li||Cu CE of all three electrolytes. The cells were cycled at 0.5 mA cm^{-2} for 1 mAh cm^{-2} and stripped to 1 V at 0.5 mA cm^{-2}. Note that prior to cycling, the copper surface is preconditioned by cycling between 0 and 1 V at 0.2 mA cm^{-2} for 10 cycles. The figure shows the CE of the first 50 cycles. The average CE values were calculated based on cycles 5 to 50, excluding the activation cycles. Four repeated cells for F2DEM, and two repeated cells for DEM and F5DEE are made, showing the consistent trend. (*D*) Li||Cu CE over 250 cycles under a fast plating (1 mA cm^{-2}) and slow stripping (0.4 mA cm^{-2}) condition. Four repeated cells for F2DEM, DEM, and F5DEE are made, showing the consistent trend. (*E*) The linear sweep voltammetry (LSV) in Li||Al cells. The leakage current of the three electrolytes was measured by sweeping up to 7 V at 1 mV s^{-1}. (*F*) Leakage current measured in Li||Al cells. LSV was first applied to the cells to sweep from open circuit voltage to 4.4 V at 1 mV s^{-1}. The cells were then held at 4.4 V for over 60 h. Two repeated cells are tested for each electrolyte and similar trend is observed. (*G*) LSV in Li||Pt cells showing improved oxidative stability compared to DEM. The leakage currents of the three electrolytes were measured by sweeping up to 7 V at 1 mV s^{-1}.

demanding condition since it has been reported that slower discharge than charge can lead to higher surface area Li morphology (40). However, this is also the condition that can best resemble the real-life battery charging and discharging condition. The improvement seen in F2DEM under a slower discharge rate potentially indicates that F2DEM can facilitate the formation of a more stable SEI. We further investigate the performance of anode-free pouch cells under 2C discharge, since slow charge and fast discharge conditions were generally implemented to enhance the Li morphology by reducing Li filament formation (40). Compared to F5DEE, F2DEM showed a higher capacity utilization and a slower capacity loss (Fig. 4 *E* and *F*). This improved capacity retention of F2DEM can be partially attributed to its low overpotential and higher ionic conductivity, which is consistent with our previous observation in Li||Li symmetric cells (Fig. 3*A*). Note that the fluctuation in CE and capacity profile under this fast discharge condition might be due to various factors including temperature fluctuation and dead Li reconnection during cycling. Under symmetric C/2 charge rate and C/2 discharge rate, 2M LiFSI/F2DEM yielded similar cycling performance as the two reference electrolytes (Fig. 4 *C* and *D*).

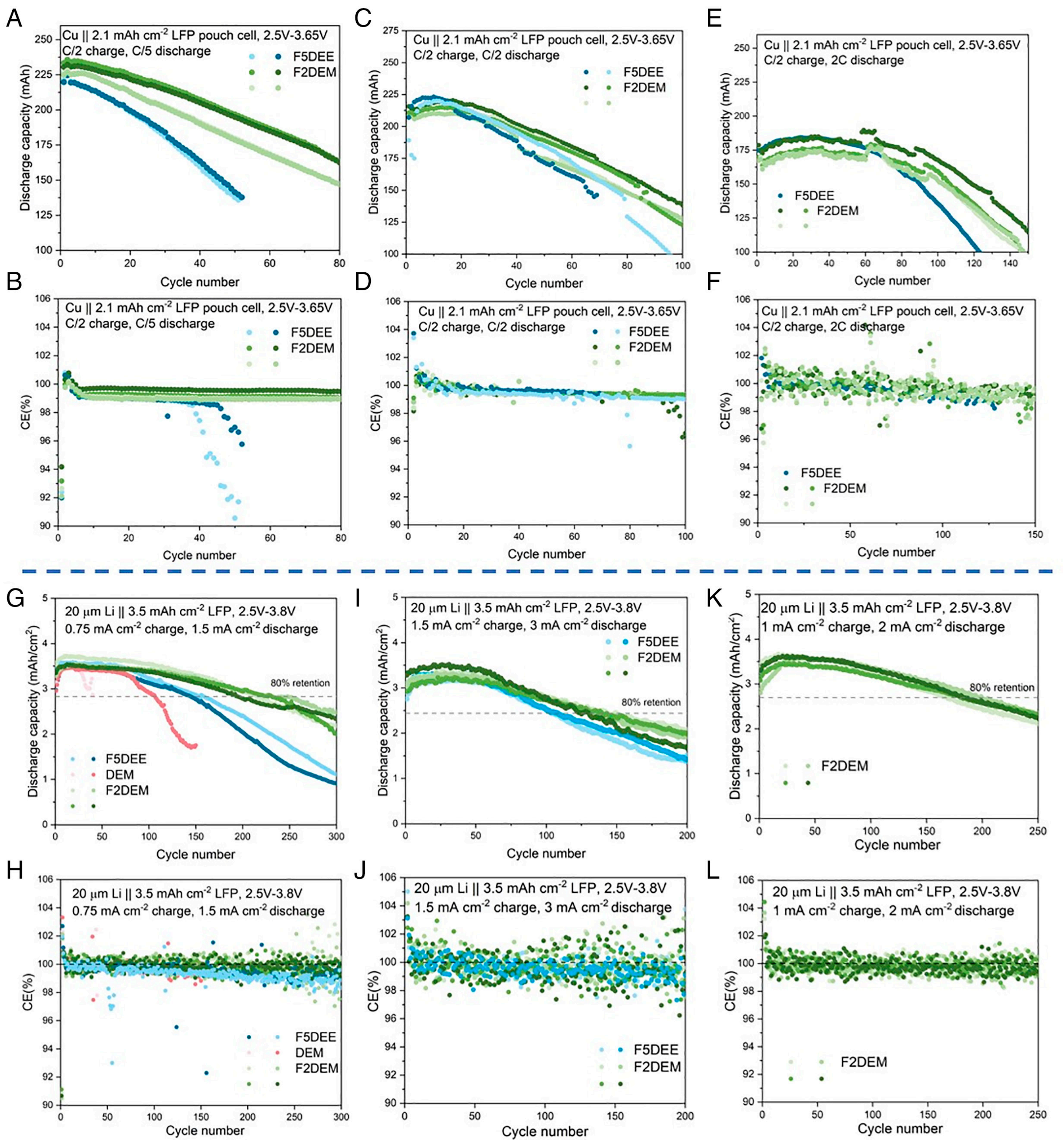

Fig. 4. (*A*–*F*) Performance of Cu||LFP pouch cell cycling between 2.5 V and 3.65 V. The nominal capacity at C/3 is 210 mAh, or 2.1 mAh cm^{-2}. The electrolyte loading is 0.5 mL. The 2M LiFSI/F2DEM is compared to 1.2M LiFSI/F5DEE and F4DEE under various charging and discharging conditions. (*A* and *B*) C/2 charge and C/5 discharge capacity (1C = 200 mA or 2 mA cm^{-2}) and CE profile over 80 cycles. Four repeated cells for F2DEM are shown. (*C* and *D*) C/2 charge and C/2 discharge capacity and CE profile over 150 cycles. Two repeated cells for F5DEE and four repeated cells for F2DEM are shown. (*E* and *F*) C/2 charge and 2C discharge capacity and CE profile over 100 cycles. Two repeated cells for F5DEE and F4DEE and four repeated cells for F2DEM are shown. The data for F4DEE and F5DEE are taken from ref. 22. (*G*–*L*) Performance of Li||LFP cells with 20-μm Li anode and high-loading 3.5 mAh cm^{-2} LFP cathode for 2M LiFSI/F2DEM, 1.2M LiFSI/F5DEE, and 2M LiFSI/DEM. The cells are cycled between 2.5 V to 3.8 V. The electrolyte loading is 40 μL. The 80% capacity retention is defined by setting the cell with highest first cycle discharge capacity as the 100% capacity reference. (*G* and *H*) Discharge capacity and CE profile of cells cycled under 0.75 mA cm^{-2} charge and 1.5 mA cm^{-2} discharge (with comparison to F5DEE and DEM). Two repeated cells for F5DEE and DEM, and four repeated cells for F2DEM are shown. (*I* and *J*) Discharge capacity and CE profile of cells cycled under 1.5 mA cm^{-2} charge and 3 mA cm^{-2} discharge (with comparison to F5DEE). Two repeated cells for F5DEE and four repeated cells for F2DEM are shown. (*K* and *L*) Discharge capacity and CE profile of F2DEM cells cycled under 1 mA cm^{-2} charge and 2 mA cm^{-2} discharge. Four repeated cells for F2DEM are shown.

This is likely because the advantage of low overpotential cannot be clearly observed under slow conditions. Overall, 2M LiFSI/F2DEM showed excellent performance in the anode-free LFP pouch cells under all tested rates, and particularly under fast charge and slow discharge condition where a more stable SEI is required to enhance the cycling stability.

Coin Cell Performance

The cycling performance of 2M LiFSI/F2DEM was also evaluated in Li||LFP coin cells with 20-μm-thick Li anode and high-loading 3.5 mAh cm^{-2} LFP cathode. The additional lithium source will allow us to probe the long-term cycling performance of Li||LFP cells. Various charge and discharge current densities (0.75 mA cm^{-2} charge and 1.5 mA cm^{-2} discharge, 1.5 mA cm^{-2} charge and 3 mA cm^{-2} discharge, 1mA cm^{-2} charge and 2 mA cm^{-2} discharge, and 0.4 mA cm^{-2} charge and 2 mA cm^{-2} discharge) were applied with 3.8 V cutoff (Fig. 4 *G–L* and *SI Appendix*, Fig. S6). With 0.75 mA cm^{-2} charge and 1.5 mA cm^{-2} discharge, a higher capacity retention was observed for F2DEM than F5DEE and DEM (Fig. 4 *G* and *H*). From the charge and discharge curves of all three electrolytes (*SI Appendix*, Fig. S7), the voltage plateau increased over cycling, indicating an increase in overpotential. However, since voltage divergence can still be observed after 150 cycles, overpotential increase should not be the only failure mechanism. The lithium inventory loss may also contribute to the capacity loss. Therefore, we hypothesize that the improved capacity retention of F2DEM is likely due to its low and stable overpotential, in combination with its formation of a more stable SEI to reduce lithium inventory loss, prolonging the cycle life of F2DEM-based cells. This hypothesis will be verified in the next section through dead Li quantification. Further increasing the current densities to 1.5 mA cm^{-2} charge and 3 mA cm^{-2} discharge, F2DEM can retain 80% of the initial capacity over 125 cycles while the capacity of F5DEE dropped below 80% retention after 100 cycles (Fig. 4 *I* and *J*). The charge and discharge curves (*SI Appendix*, Fig. S7) showed a similar trend as the 0.75 mA cm^{-2} charge and 1.5 mA cm^{-2} discharge condition, where F2DEM showed superior capacity retention with a lower overpotential increase and likely a less lithium inventory loss. DEM was not included in this comparison due to its poor performance even under slower charging conditions. The performance of F2DEM is further assessed in 1 mA cm^{-2} charge and 2 mA cm^{-2} discharge, as well as 0.4 mA cm^{-2} charge and 2 mA cm^{-2} discharge conditions, although there are no reported F5DEE comparison data for these two conditions. Under a relatively fast discharge rate of 2 mA cm^{-2}, F2DEM can retain 80% of its first cycle capacity over 200 cycles with 1 mA cm^{-2} charge rate (Fig. 4 *K* and *L*). When the charge rate was changed to 0.4 mA cm^{-2}, the cells can still achieve stable CE and 80% capacity retention over 350 cycles (*SI Appendix*, Fig. S6). These observations corroborate F2DEM's excellent stability even under high-rate conditions. We note here that despite the excellent rate performance of F2DEM, the lower degree of fluorination leads to a trade-off in oxidative stability. This makes F2DEM less compatible with higher voltage cathodes such as NMC811 (*SI Appendix*, Fig. S14). Additional studies on strategies to further improve the oxidative stability, while maintaining good transport properties will be necessary.

SEI and Dead Lithium Characterizations

The above discussion highlights the superior performance of F2DEM under various charging and discharging conditions. Of note is its excellent capacity retention under fast charge and slow discharge condition, greatly surpassing that of F5DEE and DEM. As mentioned above, this is a more critical condition tested, which is closer to the real-life battery usage demands. Considering these factors, we focus on understanding the various factors that may contribute to capacity loss among the three electrolytes under this specific condition.

Generally, capacity loss in Li||Cu cells can be attributed to either SEI or dead Li formation. To study the difference between the SEI formed in 2M LiFSI/F2DEM and 1.2M LiFSI/F5DEE, we first probe the properties of the chemically formed SEI in the studied electrolytes. The two properties we are particularly interested in are the resistivity and passivating ability of the SEI. EIS is used to characterize the initial SEI resistance and after resting for 5 d to study the corrosion behavior in different electrolytes. Among the three electrolytes, F2DEM shows the lowest initial SEI resistance, followed by DEM and F5DEE (Fig. 5*A* and *SI Appendix*, Fig. S8*A*). The SEI formed with F2DEM appears more passivating compared to F5DEE, as evident from a lesser growth in impedance of around 43% over 5 d (Fig. 5*B* and *SI Appendix*, Fig. S8 *B–D*). While F5DEE experiences 103% growth during this period, F2DEM only experiences a 43% growth. The less resistive SEI on F2DEM may enable good Li transport, which may lead to less dead Li formation as discussed in the later section. A more passivating SEI also has the benefit of causing less electrolyte consumption over time.

In addition to the impedance measurements, it is critical to understand the chemical composition of the SEI formed in the different electrolytes. XPS is thus performed on the residual SEI formed in 2M LiFSI/F2DEM and 1.2M LiFSI/F5DEE after 10 cycles under symmetric plating and stripping (0.5 mA cm^{-2}, 0.5 mA cm^{-2}, 1 mAh cm^{-2}). To obtain the depth profile, the samples are sputtered with argon for 1, 2, and 3 min. As shown in Fig. 5 *C* and *D*, no clear distinction is observed with the two electrolytes cycled under the same condition. We can identify peaks corresponding to the common SEI species, such as LiF, Li_2O, SO_x species, and Li_2S. It appears that the inorganic salt decomposition products dominate the SEI in both electrolytes, which have been seen with multiple other high-CE weakly solvating electrolytes (14, 15, 22–28). The elemental ratio analysis based on the XPS results also show comparable F/C, O/F, O/C, and S/C ratio for F2DEM and F5DEE (*SI Appendix*, Fig. S9).

With the similarities in composition, the difference in performance can potentially be traced to structural difference in the SEI. To test for this, we use FIB to cut a cross-section in the SEI formed after 20 cycles. As shown in Fig. 5*E*, the residual SEI formed in F2DEM and F5DEE appears to be similar in thickness (~3 μm) and porosity. We further use cryo-EM to examine the direct SEI thickness of the two electrolytes. Interestingly, although F2DEM shows less capacity loss due to SEI formation, thicker direct SEI is observed (Fig. 5*E* and *SI Appendix*, Fig. S10). While the thickness of direct SEI formed in F5DEE averages to be around 15 nm, the thickness is around 30 nm for F2DEM. However, we note that there is no direct correlation between direct SEI thickness and cycling performance (41). For instance, it is possible that the thicker direct SEI formed in F2DEM has better passivating ability (as shown with EIS), which can benefit Li reversibility in later cycles. Further investigations into the swelling behavior of different electrolyte systems through techniques such as quartz crystal microbalance (QCM), atomic force microscopy (AFM), and dynamic impedance spectroscopy will help elucidate this observation.

Upon studying the SEI difference of the two electrolytes, we proceed to quantify dead Li formation through titration gas chromatography (TGC) (42). In this case, we react metallic Li^0 with protic solvents to generate hydrogen gas. For this study, 1 mL H_2O is added to a 10 mL sealed vial containing the residual SEI, and the amount of H_2 gas generated is quantified via gas chromatography. With this setup, two clear trends can be observed by varying the electrolyte and cycling condition (Fig. 6*A*). Comparing between the two tested electrolytes (F2DEM and F5DEE) under the same cycling condition, F5DEE generates over two times more

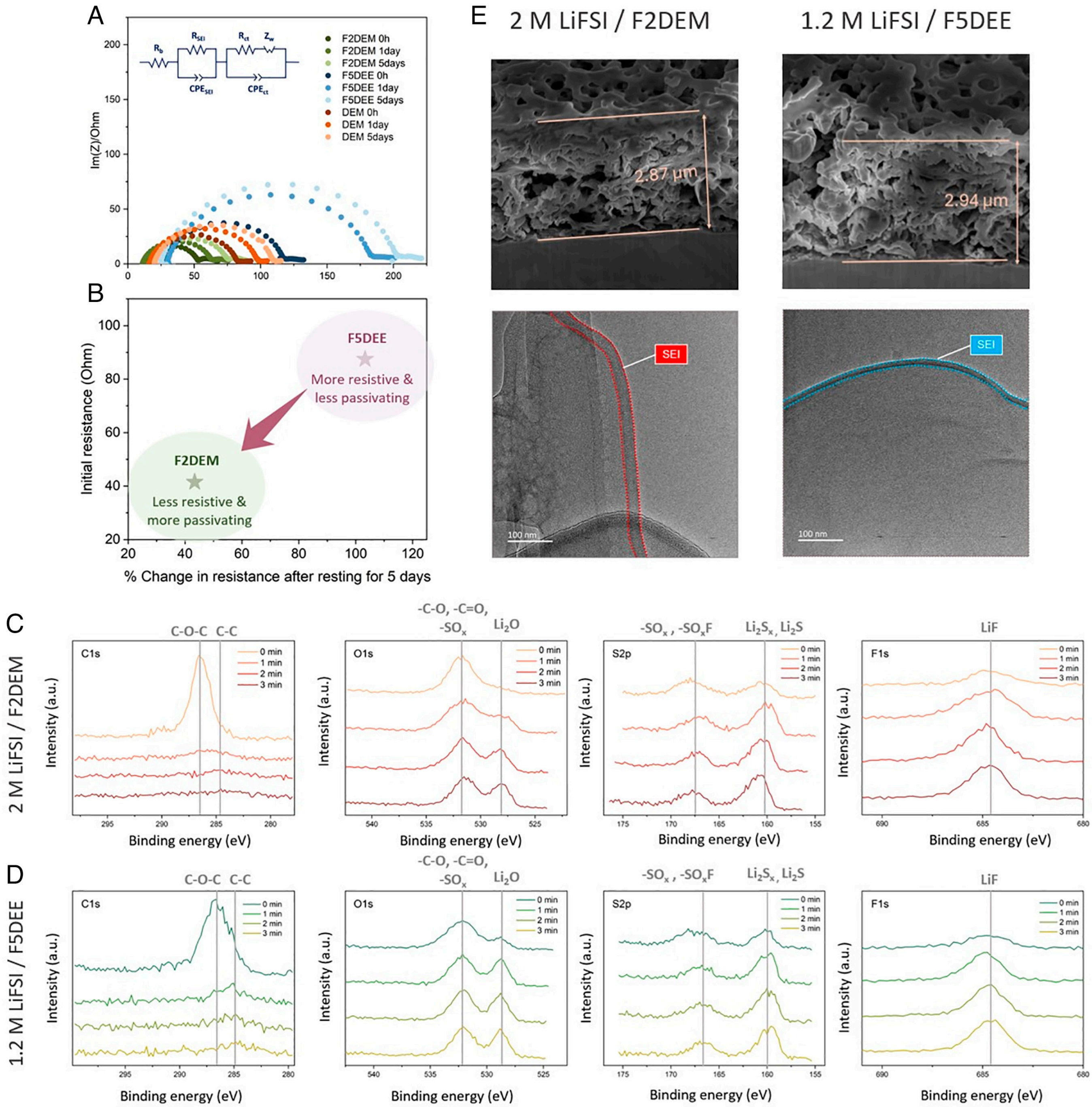

Fig. 5. (*A*) Electrochemical impedance spectroscopy (EIS) of 1.2M LiFSI/F5DEE, 2M LiFSI/F2DEM, and 2M LiFSI/DEM to study the relative resistance of the SEI formed in these electrolytes. The frequency range is 100 mHz to 1 MHz. The initial impedance curve of F2DEM and F5DEE without cycling and the change in impedance over 5 d is shown. (*B*) The initial resistance vs. percentage change in resistance after 5 d plot showing that F2DEM has a less resistive and more passivating SEI compared to F5DEE. (*C* and *D*) The X-ray photoelectron spectroscopy (XPS) depth profile of residual SEI formed after 10 cycles at 0.5 mA cm^{-2} and 1 mAh cm^{-2} in 2M F2DEM (*C*) and 1.2M F5DEE (*D*). The C1s, O1s, S2p, and F1s profiles are shown. (*E*) Cross-section images of residual SEI formed under 1 mA cm^{-2} plating and 0.4 mA cm^{-2} and 2 mAh cm^{-2} captured by focused ion beam (FIB) (*Top*), and cryo-TEM bright field images of direct SEI formed on lithium metal deposits in 1.2M LiFSI/F5DEE and 2M LiFSI/F2DEM (*Bottom*).

dead Li than F2DEM. Further changing the cycling condition from symmetric plating and stripping (0.5 mA cm^{-2}, 0.5 mA cm^{-2}, 1 mAh cm^{-2}) to fast plating and slow stripping (1 mA cm^{-2}, 0.4 mA cm^{-2}, 2 mAh cm^{-2}), more dead Li is found in the latter condition for both electrolytes. We further quantify how much dead Li contributes to the total capacity loss in both conditions for each electrolyte (Fig. 6*B*). With the assumption that capacity loss mainly comes from either SEI accumulation or dead Li formation, we calculate the SEI capacity loss by subtracting the dead Li capacity loss determined by TGC from total capacity loss over 20 cycles. This allows us to better understand the contribution from each part of the capacity loss mechanism. As shown in Fig. 6*B*, F5DEE has much more capacity loss from dead Li formation (over 50% for both conditions) compared to F2DEM (around 30%). The percentage loss from dead Li is summarized in *SI Appendix*, Table S6. The increase in dead Li capacity loss helps us to explain the lower CE of F5DEE. Interestingly, we do not observe significant difference in the SEI capacity loss in the two electrolytes. We

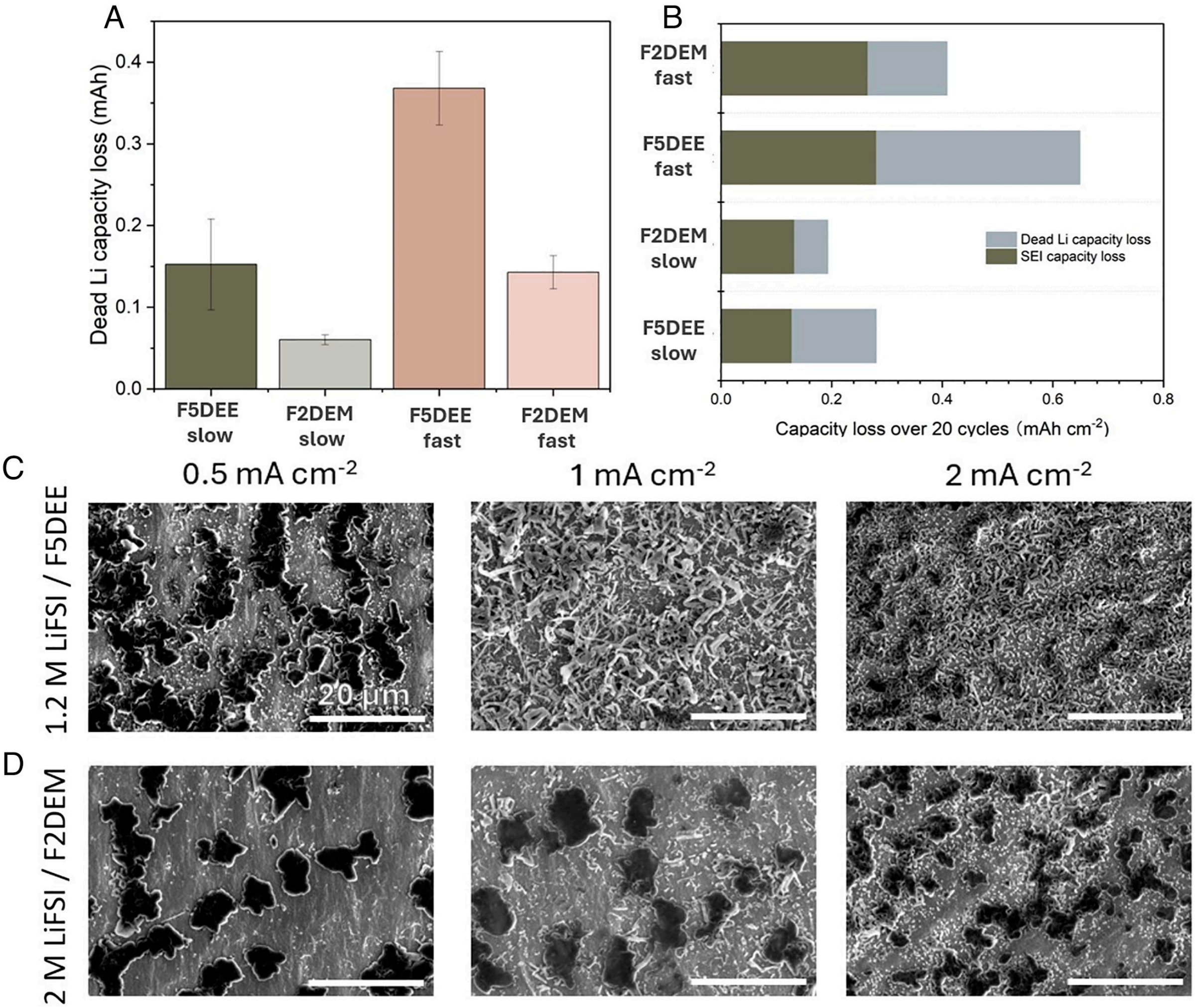

Fig. 6. (*A*) The dead Li capacity loss determined by titration gas chromatography. The dead Li capacity loss determined by titration gas chromatography of 1.2M F5DEE and 2M F2DEM under slow (0.5 mA cm^{-2} plating and stripping, 1 mAh cm^{-2}) and fast (1 mA cm^{-2} plating 0.4 mA cm^{-2} stripping, 2 mAh cm^{-2}) cycling conditions. The values are averaged among three repeat cells and error bars displayed on the plot. F2DEM shows less dead Li capacity loss under both slow and fast conditions. (*B*) SEI capacity loss calculated from total capacity loss of 1.2M F5DEE and 2M F2DEM under slow (0.5 mA cm^{-2} plating and stripping, 1 mAh cm^{-2}) and fast (1 mA cm^{-2} plating 0.4 mA cm^{-2} stripping, 2 mAh cm^{-2}) cycling conditions. (*C* and *D*) The scanning electron microscopy (SEM) images of 0.1 mAh cm^{-2} of Li deposited on copper surface in (*D*) 1.2M F5DEE and (*E*) 2M F2DEM. The Li deposits are formed at various current densities. More whisker-like morphology can be observed at higher current densities, especially for F5DEE.

also note that the dead Li capacity is calculated based on the assumption that the only source for H_2 gas is metallic Li. Considering that any LiH in the SEI may also react with water to form H_2 gas, further studies to quantify the amount of LiH may advance our understandings of the SEI property differences among the investigated electrolytes.

To further trace the origin of reduced dead Li capacity loss in F2DEM, we examine the Li deposition morphology under various current densities. In this case, we only plate a small capacity of Li (0.1 mAh cm^{-2}) to ensure the best representation of Li deposition morphology. As shown in Fig. 6 *C* and *D* and *SI Appendix*, Fig. S11, the Li morphology is similar in F2DEM and F5DEE at 0.5 mA cm^{-2}. However, as we increase the current density to 1 mA cm^{-2} and 2 mA cm^{-2}, there is a clear distinction between the two electrolytes. The Li deposition appears much chunkier in F2DEM, whereas F5DEE has more whisker-like Li morphology. To ensure that this effect stems from solvent property difference and not concentration difference of the two electrolytes, we also confirmed the morphology of deposited Li in 2M F5DEE electrolyte (*SI Appendix*, Fig. S12). This difference in Li deposition morphology can explain why more dead Li is formed with F5DEE, since the whisker growth in F5DEE is more prone to losing structural connection, leading to an increased amount of isolated (dead) Li (42).

Conclusion

In summary, we have demonstrated that the monofluorinated acetal electrolyte (F2DEM) significantly enhances the cycling stability of LMBs and have systematically investigated the underlying factors contributing to its excellent performance. The weakly solvating acetal backbone promotes a stable solid electrolyte interface (SEI) formation and lower overpotential, while the monofluorine substitution on the end carbons further improves oxidation stability, ionic conductivity, and Li passivation. These modifications enabled high Li CEs and stable long-term cycling in Li||Cu half cells, anode-free LFP pouch cells, and high-loading LFP coin cells, even under fast plating and slow stripping conditions. Furthermore, we observed improved Li deposition morphology and much reduced dead Li formation even compared to the state-of-the-art F5DEE electrolyte. Overall, our work highlights the importance of backbone modification and careful control of fluorination in electrolyte engineering. Leveraging these insights into the design of F2DEM not only advances our understanding of the interplay between electrolyte structure and battery performance but also offers a promising avenue for the development of high-energy-density LMBs.

Materials and Methods

General Materials. F5DEE was synthesized based on the procedure reported previously (22) and provided by Feon Energy. 2-Fluoroethanol was purchased from Matrix Scientific. 2,2-Difluoroethanol was purchased from SynQuest. NaOH, tetraglyme, dibromomethane, DEM, and other general reagents were purchased from Sigma Aldrich or Fisher. The separator Celgard 2325 (25-μm thick, polypropylene/polyethylene/polypropylene) was purchased from Celgard. Thick Li foil (roughly 750-μm thick) and Cu current collector (25-μm thick) were purchased from Alfa Aesar. Thin Li foils (roughly 50- and 20-μm thick, supported on Cu substrate) were purchased from China Energy Lithium. Commercial LFP cathode sheets were purchased from Targray. Industrial dry Cu||LFP pouch cells were purchased from Li-Fun Technology. Additional battery components, including 2032-type coin-cell cases, springs, and spacers, were obtained from MTI. All materials were used as received.

Electrolyte Synthesis. To a 500 mL round flask was added 64 g of 2-fluoroethanol, 85 g of dibromomethane, 43 g of NaOH, and 200 mL tetraglyme. Note that toxicity precaution is needed when handling 2-fluoroethanol. The suspension was stirred at room temperature for 2 h under air and then heated to 40 °C to stir overnight. The suspension turned brownish with yellow fine powder. The suspension was further heated to 70 °C to stir overnight. The suspension was directly distilled under vacuum (vapor temperature ~70-75 °C at ~1 kPa) to obtain colorless liquid as the product. The crude product was distilled under vacuum for four times to ensure purity. The ^{1}H and ^{19}F NMR of the purified product can be found in *SI Appendix*, Fig. S13.

Electrochemical Measurements and Characterizations. All battery components used in this work were commercially available, and all electrochemical tests were carried out using 2032-type coin cells. The cells were fabricated in an argon-filled glovebox, and one layer of Celgard 2325 was used as a separator for all batteries. Thick Li foil (750 μm) with a diameter of 7/16 in. was used for cell assembly unless otherwise specified, and 40 μL of electrolyte was injected in all cells with Cu||LFP as an exception. Both the ionic conductivity and transport number of the electrolytes were measured with Biologic VSP system. Ionic conductivity was derived from bulk impedance in symmetric cells with two stainless steel electrodes and electrolyte soaked separator. Li^+ transport number was obtained by a Li||Li symmetric cell under a polarization potential of 10 mV. Li||Cu, Li||Li, Li||LFP cells were tested on Land battery testing station, and Cu||LFP pouch cells were tested on Arbin. All cells are tested under room temperature. The Li||Li cells were cycled under different charge and discharge current densities (1 mA cm^{-2}, 4 mA cm^{-2}, 6 mA cm^{-2}, and 8 mA cm^{-2}). The CEs of the electrolytes were measured based on a modified Aurbach method (36) in Li||Cu cells, where 5 mAh cm^{-2} of Li was first deposited onto the Cu foil as Li reservoir. This was followed by 10 subsequent cycles of plating and stripping at 0.5 mA cm^{-2} for 1 mAh cm^{-2}. Finally, all deposited Li was stripped from Cu, and the total capacity recovered was divided by the amount deposited to obtain the CE. The long-term Li||Cu cycling was carried out by first conditioning the Cu surface through cycling between 0 to 1 V at 0.2 mA cm^{-2} for 10 cycles. Upon preconditioning the Cu, 1 mAh cm^{-2} of Li was plated on the Cu at 0.5 mA cm^{-2} and stripped to 1 V at the same rate. A faster plating and slower stripping condition was also used to further evaluate the cells, where 2 mAh cm^{-2} of Li was plated on Cu at 1 mA cm^{-2} and stripped to 1 V at 0.4 mA cm^{-2}. The LSV was also carried out in Li||Al and Li||Pt cells using Biologic VSP300. In both setups, the voltage was swept from open-circuit value to 7 V vs. Li^+/Li at 1 mV s^{-1}. The leakage current was evaluated by dividing the measured value by the electrode area of 2.11 cm^{-2}. Al corrosion tests were carried out in Li||Al cells, where the voltage is held at 4.4 V for over 60 h. The Cu||LFP pouch cells were tested with 0.5 mL electrolyte injected into the purchased cells. The pouch cells were clamped in woodworking vises to ensure an estimated pressure of 1,000 kPa and cycled under various charge and discharge conditions between 2.5 V and 3.65 V. The Li||LFP coin cells were assembled with 20 μm Li and 3.5 mAh cm^{-2} LFP. The cells were cycled between 2.5 V and 3.8 V under different rates after a formation cycle at 0.4 mA cm^{-2} charge and 1.5 mA cm^{-2}/3 mA cm^{-2} discharge currents. The Al-clad cathode cases were also used for Li||LFP coin cells, any defects in the Al cladding are expected to be minimized with Al foil inserted in the cathode case.

For EIS measurements, BioLogic is used, and the impedance curve is generated by scanning from a frequency of 100 mHz to 1 MHz. To carry out the XPS (PHI VersaProbe 4), the samples are pumped in the chamber overnight to ensure complete solvent removal. The sample is then vacuum transferred into the main chamber to minimize air and moisture contact. The depth profile is generated with argon sputtering for three times, with 1-min duration each time. All the SEM images are generated using Thermo Fisher Scientific Apreo S LoVac Scanning Electron Microscope at 5 kV, 50 pA. For cryo-TEM imaging, a 400-mesh Cu TEM grid was positioned on top of the Cu current collector in the coin-cell stack. After lithium plating, the cell was deconstructed inside an Ar-filled glove box to prevent exposure to air and moisture. The grid was rinsed with 1,2-dimethoxyethane (DME) to remove excess salts and then allowed to dry inside the glove box for approximately 120 s. The grid was then quickly (~2 s) transferred from the glove box in a sealed plastic Falcon tube and immediately immersed in liquid nitrogen (LN_2). Pliers were used to break open the tube under LN_2, and the Cu grid was transferred to an LN_2 dewar. While submerged in LN_2, the grid was carefully placed into a cryoholder (Gatan 626) using a cryotransfer station to ensure an air-free transfer. The cryoholder was swiftly (~1 s) removed from the transfer station and inserted into the TEM column. During imaging, the temperature was maintained at −172 °C. All cryo-TEM imaging was conducted using an FEI Titan 80-300 environmental (scanning) TEM, equipped with an aberration corrector in the objective lens. Imaging was performed at an accelerating voltage of 300 kV, with full alignments completed prior to each session to ensure optimal imaging conditions.

The dead lithium content is determined using titration gas chromatography (TGC), where the cells are first cycled 20 times before it is taken apart to remove the Cu electrode. This Cu foil (with residual SEI and dead Li) is then placed into a 10 mL GC vial inside the glovebox. This vial is properly sealed prior to taking outside of the glovebox. Then, 1 mL of water is added to each vial containing the Cu and the sample is left to react with the water for 3 min. After 3 min of reaction time, 1.5 mL of gas is drawn out of the vial and analyzed using GC.

Molecular Simulations. Classical, fixed-charge MD was conducted using LAMMPS from initial amorphous configurations with ~500 molecules with compositions corresponding to the experimentally investigated systems. The solvents, Li^+, and FSI^- were described using the General Amber forcefield. Van der Waals interactions not explicitly specified in the forcefields were generated using Lorentz-Berthelot mixing rules. In all cases, the charges of the Li^+ and FSI^- molecules were scaled to 0.75. A 10 Å cutoff for Van der Waals and real space coulomb was applied. The reciprocal space coulomb interactions were computed with a particle–particle–particle–mesh solver, with an error tolerance of 10^{-6}. Periodic boundary conditions were applied in all directions.

For each system, an initial energy minimization at 0 K (energy and force tolerances of 10^{-4}) was performed to obtain the ground-state structure. After this, the system was slowly heated from 0 K to room temperature at constant volume over 0.01 ns using a Langevin thermostat, with a damping parameter of 100 ps. Five cycles of quench-annealing dynamics were then applied in an attempt to eliminate any metastable solvation states, where the system temperature was cycled between 298 K and 894 K with a ramp period 0.025 ns followed by 0.1 ns of dynamics at either temperature extreme at constant volume. Next, in an attempt to achieve equilibration in system density, a constant temperature, constant pressure ensemble was applied using the Andersen barostat for 1.5 ns with a pressure relaxation constant of 1 ps. Finally, we performed 10 ns of constant volume, constant temperature (NVT) production dynamics at 298 K. Radial distribution functions were obtained during this period. Snapshots of the various solvation shells, sampled from the simulation trajectory, were also obtained using Visual MD (VMD) software.

Quantum chemistry simulations were performed using the Q-Chem 5.1 quantum chemistry package at the B3LYP//6-31+G(d, p) level of theory for geometry optimization and the B3LYP//6-311++G** level of theory for single-point energy calculations.

Data, Materials, and Software Availability. All study data are included in the article and/or *SI Appendix*.

ACKNOWLEDGMENTS. The work was supported by the Assistant Secretary for Energy Efficiency and Renewable Energy, Office of Vehicle Technologies of the U.S. Department of Energy under the Battery 500 Consortium program. E.Z. acknowledges the support from the NSF Graduate Research Fellowship Program (NSF GRFP). Y. Chen acknowledges the support from the Chevron Fellowship. Part of this work was performed at the Stanford Nano Shared Facilities, supported by the NSF under Award ECCS−2026822. S.C.K. acknowledges support from the Stanford Energy Postdoctoral Fellowship.

Author affiliations: [a]Department of Chemical Engineering, Stanford University, Stanford, CA 94305; [b]Department of Materials Science and Engineering, Stanford University, Stanford, CA 94305; [c]Department of Chemistry, Stanford University, Stanford, CA 94305; and [d]Stanford Institute for Materials and Energy Sciences, Stanford Linear Accelerator Center National Accelerator Laboratory, Menlo Park, CA 94025

Author contributions: E.Z., Y. Chen, Z.Y., Y. Cui, and Z.B. designed research; E.Z., Y. Chen, W.Z., H.L., I.R.C., and S.C.K. performed research; E.Z., Y. Chen, J.H., Z.Y., W.Z., H.L., I.R.C., S.C.K., and C.S. contributed new reagents/analytic tools; E.Z., Y. Chen, J.H., and C.S. analyzed data; and E.Z., Y. Chen, and J.H. wrote the paper.

1. Y. Cao, M. Li, J. Lu, J. Liu, K. Amine, Bridging the academic and industrial metrics for next-generation practical batteries. *Nat. Nanotechnol.* **14**, 200–207 (2019), 10.1038/s41565-019-0371-8.
2. P. Albertus, S. Babinec, S. Litzelman, A. Newman, Publisher correction: Status and challenges in enabling the lithium metal electrode for high-energy and low-cost rechargeable batteries. *Nat. Energy* **7**, 899–899 (2022), 10.1038/s41560-022-01077-8.
3. J. Liu *et al.*, Pathways for practical high-energy long-cycling lithium metal batteries. *Nat. Energy* **4**, 180–186 (2019), 10.1038/s41560-019-0338-x.
4. G. M. Hobold *et al.*, Moving beyond 99.9% Coulombic efficiency for lithium anodes in liquid electrolytes. *Nat. Energy* **6**, 951–960 (2021), 10.1038/s41560-021-00910-w.
5. M. D. Tikekar, S. Choudhury, Z. Tu, L. A. Archer, Design principles for electrolytes and interfaces for stable lithium-metal batteries. *Nat. Energy* **1**, 16114 (2016), 10.1038/nenergy.2016.114.
6. D. Lin, Y. Liu, Y. Cui, Reviving the lithium metal anode for high-energy batteries. *Nat. Nanotechnol.* **12**, 194–206 (2017), 10.1038/nnano.2017.16.
7. J. Xiao *et al.*, Understanding and applying coulombic efficiency in lithium metal batteries. *Nat. Energy* **5**, 561–568 (2020), 10.1038/s41560-020-0648-z.
8. H. Adenusi, G. A. Chass, S. Passerini, K. V. Tian, G. Chen, Lithium batteries and the solid electrolyte interphase (SEI)—Progress and outlook. *Adv. Energy Mater.* **13**, 2203307 (2023), 10.1002/aenm.202203307.
9. A. Wang, S. Kadam, H. Li, S. Shi, Y. Qi, Review on modeling of the anode solid electrolyte interphase (SEI) for lithium-ion batteries. *npj Comput. Mater.* **4**, 15 (2018), 10.1038/s41524-018-0064-0.
10. N. Aspern, G.-V. Röschenthaler, M. Winter, I. Cekic-Laskovic, Fluorine and lithium: Ideal partners for high-performance rechargeable battery electrolytes. *Angew. Chem. Int. Ed.* **58**, 15978–16000 (2019), 10.1002/anie.201901381.
11. X. Fan, C. Wang, High-voltage liquid electrolytes for Li batteries: Progress and perspectives. *Chem. Soc. Rev.* **50**, 10486–10566 (2021), 10.1039/D1CS00450F.
12. Z. Yu *et al.*, Molecular design for electrolyte solvents enabling energy-dense and long-cycling lithium metal batteries. *Nat. Energy* **5**, 526–533 (2020), 10.1038/s41560-020-0634-5.
13. Y. Yamada, J. Wang, S. Ko, E. Watanabe, A. Yamada, Advances and issues in developing salt-concentrated battery electrolytes. *Nat. Energy* **4**, 269–280 (2019), 10.1038/s41560-019-0336-z.
14. X. Cao, H. Jia, W. Xu, J.-G. Zhang, Review—Localized high-concentration electrolytes for lithium batteries. *J. Electrochem. Soc.* **168**, 010522 (2021), 10.1149/1945-7111/abd60e.
15. X. Ren *et al.*, Enabling high-voltage lithium-metal batteries under practical conditions. *Joule* **3**, 1662–1676 (2019), 10.1016/j.joule.2019.05.006.
16. H. Zhang *et al.*, Electrolyte additives for lithium metal anodes and rechargeable lithium metal batteries: Progress and perspectives. *Angew. Chem. Int. Ed.* **57**, 15002–15027 (2018), 10.1002/anie.201712702.
17. J. Holoubek *et al.*, An all-fluorinated ester electrolyte for stable high-voltage Li metal batteries capable of ultra-low-temperature operation. *ACS Energy Lett.* **5**, 1438–1447 (2020), 10.1021/acsenergylett.0c00643.
18. J. Chen *et al.*, Electrolyte design for Li metal-free Li batteries. *Mater. Today* **39**, 118–126 (2020), 10.1016/j.mattod.2020.04.004.
19. R. Weber *et al.*, Long cycle life and dendrite-free lithium morphology in anode-free lithium pouch cells enabled by a dual-salt liquid electrolyte. *Nat. Energy* **4**, 683–689 (2019), 10.1038/s41560-019-0428-9.
20. A. J. Louli *et al.*, Diagnosing and correcting anode-free cell failure via electrolyte and morphological analysis. *Nat. Energy* **5**, 693–702 (2020), 10.1038/s41560-020-0668-8.
21. Y. Chen *et al.*, Steric effect tuned ion solvation enabling stable cycling of high-voltage lithium metal battery. *J. Am. Chem. Soc.* **143**, 18703–18713 (2021), 10.1021/jacs.1c09006.
22. Z. Yu *et al.*, Rational solvent molecule tuning for high-performance lithium metal battery electrolytes. *Nat. Energy* **7**, 94–106 (2022), 10.1038/s41560-021-00962-y.
23. C. V. Amanchukwu *et al.*, A new class of ionically conducting fluorinated ether electrolytes with high electrochemical stability. *J. Am. Chem. Soc.* **142**, 7393–7403 (2020), 10.1021/jacs.9b11056.
24. X. Cao *et al.*, Effects of fluorinated solvents on electrolyte solvation structures and electrode/electrolyte interphases for lithium metal batteries. *Proc. Natl. Acad. Sci. U.S.A.* **118**, e2020357118 (2021), 10.1073/pnas.2020357118.
25. Y. Zhao *et al.*, Fluorinated ether electrolyte with controlled solvation structure for high voltage lithium metal batteries. *Nat. Commun.* **13**, 2575 (2022), 10.1038/s41467-022-29199-3.
26. G. Zhang *et al.*, A monofluoride ether-based electrolyte solution for fast-charging and low-temperature non-aqueous lithium metal batteries. *Nat. Commun.* **14**, 1081 (2023), 10.1038/s41467-023-36793-6.
27. Y. Zhao, T. Zhou, M. Mensi, J. W. Choi, A. Coskun, Electrolyte engineering via ether solvent fluorination for developing stable non-aqueous lithium metal batteries. *Nat. Commun.* **14**, 299 (2023), 10.1038/s41467-023-35934-1.
28. D. Ruan *et al.*, Solvent versus anion chemistry: unveiling the structure-dependent reactivity in tailoring electrochemical interphases for lithium-metal batteries. *JACS Au* **3**, 953–963 (2023), 10.1021/jacsau.3c00035.
29. S. Jiao *et al.*, Stable cycling of high-voltage lithium metal batteries in ether electrolytes. *Nat. Energy* **3**, 739–746 (2018), 10.1038/s41560-018-0199-8.
30. X. Ren *et al.*, High-concentration ether electrolytes for stable high-voltage lithium metal batteries. *ACS Energy Lett.* **4**, 896–902 (2019), 10.1021/acsenergylett.9b00381.
31. S. Chen *et al.*, Strongly solvating ether electrolytes for high-voltage lithium metal batteries. *ACS Appl. Mater. Interfaces* **10**, 13155–13164 (2023), 10.1021/acsami.3c00165.
32. K. M. Wollin *et al.*, PFASs-restriction proposal commentary on ECHA's Annex XV restriction report, proposal for a restriction, March 2023. *Arch Toxicol* **97**, 3305–3312 (2023), 10.1007/s00204-023-03597-y.
33. Y. Chen *et al.*, Hyperconjugation-controlled molecular conformation weakens lithium-ion solvation and stabilizes lithium metal anode. ChemRxiv [Preprint] (2024). https://doi.org/10.26434/chemrxiv-2024-96jh5 (Accessed 10 August 2024).
34. G. A. Giffin, The role of concentration in electrolyte solutions for non-aqueous lithium-based batteries. *Nat. Commun.* **13**, 5250 (2022), 10.1038/s41467-022-32794-z.
35. S. C. Kim *et al.*, Potentiometric measurement to probe solvation energy and its correlation to lithium battery cyclability. *J. Am. Chem. Soc.* **143**, 10301–10308 (2021), 10.1021/jacs.1c03868.
36. B. D. Adams, J. Zheng, X. Ren, W. Xu, J. Zhang, Accurate determination of coulombic efficiency for lithium metal anodes and lithium metal batteries. *Adv. Energy Mater.* **8**, 1702097 (2018), 10.1002/aenm.201702097.
37. D. Aurbach, Y. Gofer, J. Langzam, The correlation between surface chemistry, surface morphology, cycling efficiency of lithium electrodes in a few polar aprotic systems. *J. Electrochem. Soc.* **136**, 3198–3205 (1989), 10.1149/1.2096425.
38. W. Xue *et al.*, Ultra-high-voltage Ni-rich layered cathodes in practical Li metal batteries enabled by a sulfonamide-based electrolyte. *Nat. Energy* **6**, 495–505 (2021), 10.1038/s41560-021-00792-y.
39. T. Ma *et al.*, Revisiting the corrosion of the aluminum current collector in lithium-ion batteries. *J. Phys. Chem. Lett.* **8**, 1072–1077 (2017), 10.1021/acs.jpclett.6b02933.
40. A. J. Louli *et al.*, Optimizing cycling conditions for anode-free lithium metal cells. *J. Electrochem. Soc.* **168**, 020515 (2021), 10.1149/1945-7111/abe089.
41. Z. Zhang *et al.*, Capturing the swelling of solid-electrolyte interphase in lithium metal batteries. *Science* **375**, 66–67 (2022), 10.1126/science.abi8703.
42. C. Fang *et al.*, Quantifying inactive lithium in lithium metal batteries. *Nature* **572**, 511–515 (2019), 10.1038/s41586-019-1481-z.